Biaxial ferromagnetic liquid crystal colloids

Qingkun Liu[a], Paul J. Ackerman[a,b], Tom C. Lubensky[c], and Ivan I. Smalyukh[a,b,d,e,f,1]

[a]Department of Physics, University of Colorado, Boulder, CO 80309; [b]Department of Electrical, Computer and Energy Engineering, University of Colorado, Boulder, CO 80309; [c]Department of Physics and Astronomy, University of Pennsylvania, Philadelphia, PA 19104; [d]Materials Science and Engineering Program, University of Colorado, Boulder, CO 80309; [e]Soft Materials Research Center, University of Colorado, Boulder, CO 80309; and [f]Renewable and Sustainable Energy Institute, National Renewable Energy Laboratory and University of Colorado, Boulder, CO 80309

Edited by David A. Weitz, Harvard University, Cambridge, MA, and approved July 26, 2016 (received for review January 22, 2016)

The design and practical realization of composite materials that combine fluidity and different forms of ordering at the mesoscopic scale are among the grand fundamental science challenges. These composites also hold a great potential for technological applications, ranging from information displays to metamaterials. Here we introduce a fluid with coexisting polar and biaxial ordering of organic molecular and magnetic colloidal building blocks exhibiting the lowest symmetry orientational order. Guided by interactions at different length scales, rod-like organic molecules of this fluid spontaneously orient along a direction dubbed "director," whereas magnetic colloidal nanoplates order with their dipole moments parallel to each other but pointing at an angle to the director, yielding macroscopic magnetization at no external fields. Facile magnetic switching of such fluids is consistent with predictions of a model based on competing actions of elastic and magnetic torques, enabling previously inaccessible control of light.

self-assembly | ferromagnetism | nematic | colloidal dispersion

Liquid crystals (LCs) that combine fluidity with many forms of orientational and partial positional order are ubiquitous (1, 2). Fluids with polar ordering were envisaged by Born a century ago (3–5), with their study recently guided by prescient theories of Brochard and de Gennes (6–12). An experimental search for small-molecule biaxial nematic fluids has gone on for decades (2, 13). Many types of low-symmetry ordering have been found in smectic and columnar systems (14, 15) with fluidity in only two and one dimensions, respectively (1). However, nematic LCs with 3D fluidity and no positional order tend to be nonpolar, although phases with polar and biaxial structure have been considered (15–17). In colloids, such as aqueous suspensions of rods and platelets, nonpolar uniaxial ordering is also predominant (1, 18). At the same time, there is a great potential for guiding low-symmetry assembly in hybrid LC-colloidal systems, in which the molecular LC is a fluid host for colloidal particles (18). Different types of LC-mediated ordering of anisotropic particles can emerge from elastic and surface-anchoring-based interactions and can lead to the spontaneous polar alignment of magnetic inclusions (6), although the orientations of the magnetic dipoles of colloidal particles were always slave to the LC director $\mathbf{n}$, orienting either parallel or perpendicular to it without breaking uniaxial symmetry (6–12).

In this work, by controlling surface anchoring of colloidal magnetic nanoplates in a nematic host, we decouple the polar ordering of magnetic dipole moments described by macroscopic magnetization $\mathbf{M}$ from the nonpolar director $\mathbf{n}$ describing the orientational ordering of the LC host molecules. The ensuing biaxial ferromagnetic LC colloids (BFLCCs) possess 3D fluidity and simultaneous polar ferromagnetic and biaxial order. Direct imaging of nanoplates and their magnetic moment orientations relative to $\mathbf{n}$ and holonomic control of fields that strongly couple to $\mathbf{M}$ and reveal their orientations, as well as numerical modeling and optical characterization, provide the details of molecular and colloidal self-organization and unambiguously establish that BFLCCs have C_s (also denoted C_{1h}) symmetry. This symmetry, which has three distinct axes and is thus biaxial, is lower than the orthorhombic D_{2h} symmetry of conventional biaxial nematics (13) and other partially ordered molecular and colloidal fluids (1, 2, 17). We explore polar switching of this system and describe its unusual domain structures. We discuss potential applications and foresee exciting science emerging from the new soft matter framework that the BFLCCs introduce.

Results and Discussion

Our experiments use ferromagnetic nanoplates (FNPs) with average lateral size 140 nm and thickness 7 nm (12) coated with thin (<6 nm) layers of silica and surface-functionalized with polymer (19) to yield conically degenerate surface boundary conditions for $\mathbf{n}$ (20) (Fig. 1 *A* and *B* and Fig. S1). FNPs spontaneously orient with their magnetic dipole moments $\mathbf{m}$, which are normal to their large-area faces, tilted by an angle θ_{me} with respect to the far-field director $\mathbf{n}_0$ (Fig. 1*C*), as dictated by minimization of the surface anchoring free energy arising from the conical boundary conditions imposed by polymer surface functionalization (20). By inducing electrophoretic motion of FNPs in response to an electric field, with the electrophoretic and the viscous drag forces balanced, and by independently estimating the viscous drag coefficient through characterization of Brownian motion (Fig. S2), we find that FNPs have negative surface charge in the range of 100–500e per particle, where $e \approx 1.6 \times 10^{-19}$ C (*Supporting Information*) (21). Stabilized against aggregation by weakly screened electrostatic repulsions in the LC due to nanoplate charging, FNPs uniformly disperse and form BFLCCs at concentrations ~1 wt % (~0.2 vol %) and higher (Fig. 1*D*). Salient properties of BFLCCs include magnetic hysteresis and threshold-free polar switching (Figs. 1 *E* and *F* and 2). Hysteresis loops are observed for both homeotropic (Fig. 2 *A*, *C*, and *D*) and planar (Fig. 2*E*) cells with $\mathbf{n}_0$ perpendicular and parallel to confining substrates, respectively, as well as for orientations of applied field $\mathbf{B}$ and measured $\mathbf{M}$-components parallel and perpendicular to $\mathbf{n}_0$. Resisted by elastic energy costs of director distortions, magnetic switching of single-domain BFLCCs is threshold-free for fields applied in directions parallel and perpendicular to $\mathbf{n}_0$ and is different from that of uniaxial ferromagnetic LC colloids (6–12). The field $\mathbf{B}\|\mathbf{n}_0$ applied to a BFLCC with $\mathbf{n}_0$ along the cell normal $\mathbf{z}$, with a tilted $\mathbf{M}$ spontaneously along one of the orientations on the up-cone, rotates $\mathbf{M}$ toward $\mathbf{B}$ and thereby tilts the director away from the confining surface normal, leading to light transmission through the sample placed between crossed polarizers (Fig. 2*B*). The angle θ_n

Significance

We introduce a soft-matter system with fluidity coexisting with long-range biaxial and ferromagnetic ordering of anisotropic molecular and magnetic colloidal building blocks. The facile polar switching of this complex fluid promises technological applications and rich physical behavior arising from the properties of solid magnetic nanoparticles and their long-range ordering prompted by interactions with the host medium.

Author contributions: I.I.S. designed research; Q.L., P.J.A., T.C.L., and I.I.S. performed research; Q.L., and I.I.S. analyzed data; and Q.L., and I.I.S. wrote the paper.

The authors declare no conflict of interest.

This article is a PNAS Direct Submission.

[1] To whom correspondence should be addressed. Email: ivan.smalyukh@colorado.edu.

This article contains supporting information online at www.pnas.org/lookup/suppl/doi:10.1073/pnas.1601235113/-/DCSupplemental.

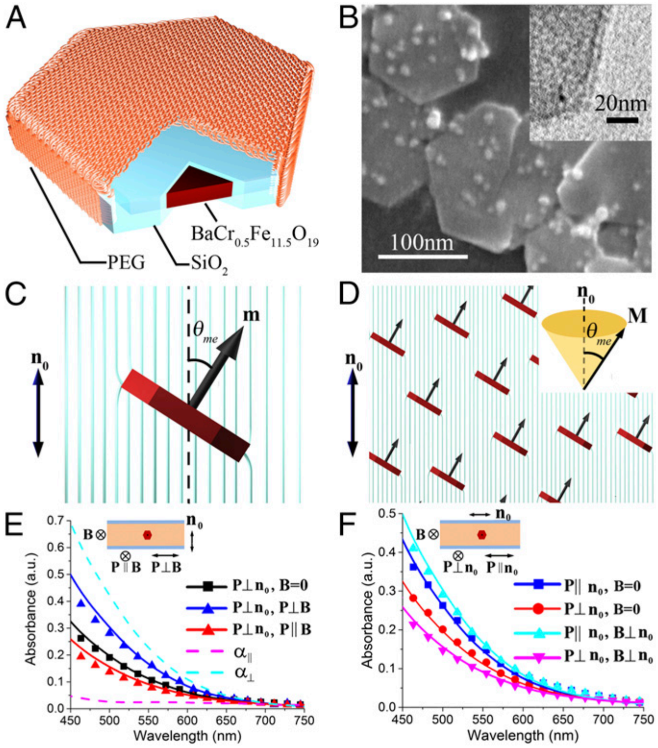

Fig. 1. BFLCCs formed by collectively tilted FNPs in an LC. (*A*) Schematic of the FNP. (*B*) Scanning TEM image of FNPs and a zoomed-in TEM image of a nanoplate's edge revealing ~5-nm-thick silica shell (*Inset*). (*C*) Schematic of an FNP in LC. (*D*) BFLCC with **M** tilted with respect to $\mathbf{n_0}$. (*E* and *F*) Experimental (symbols) and theoretical (solid curves) polarized absorption spectra for linear polarizations **P**, revealing alignment of FNPs without and with B = 2 mT in (*E*) homeotropic and (*F*) planar cells. Pure absorbances $\alpha_\perp$ and $\alpha_\parallel$ of FNPs were calculated from experimentally measured values described in ref. 10 for **P**⊥**m** and **P**∥**m**, respectively.

between the BFLCC director **n** and **z** in the middle of a homeotropic cell increases up to θ_{me} (Fig. 2 *F* and *G*). Reversal of **B** causes a much more dramatic response of the BFLCC between crossed polarizers mediated by a strong reorientation of **M** and **n** (Fig. 2*B*), with θ_n increasing above 90° at strong fields rather than saturating at θ_{me} (Fig. 2 *F* and *G*). For a BFLCC with the down-cone orientation of **M** with respect to $\mathbf{n}_0$ this behavior is completely reversed but consistent from the standpoint of the mutual orientations of **B**, **M**, and $\mathbf{n}_0$, showing that switching is polar (Fig. 2*B*) but different from that of uniaxial ferromagnetic LC colloids (9–12). BFLCCs exhibit hysteresis for **M**-components parallel and perpendicular to $\mathbf{n}_0$ (Fig. 2 *A* and *C*–*E*).

We explore FNP-LC dispersions starting from individual particles. The surface anchoring energy per FNP as a function of angle θ_m between **m** and $\mathbf{n}_0$ can be found by integrating the energy density $W_s(\theta_m)$, characterized by the conical anchoring coefficient A (20), over the surface area σ of FNP with radius R while neglecting contributions of side faces:

$$F_s = \int_\sigma W_s(\theta_m)dS = \pi AR^2\left(\cos^2\theta_m - \cos^2\theta_{me}\right)^2/2. \qquad [1]$$

Magnetic fields can rotate FNPs and **m** away from the minimum-energy orientation at $\theta_m = \theta_{me}$, as discussed by Brochard and de Gennes (6) in the one-elastic-constant (K) approximation while accounting for the energetic costs of rotation-induced elastic distortions for infinitely strong anchoring. By extending this model to the case of finite-strength conically degenerate boundary conditions (Fig. 3*A*), we find the total elastic and surface anchoring energy cost of rotating the FNP away from the equilibrium orientation for small $\theta_m - \theta_{me}$:

$$F_{se} \approx 4\pi KAR^2\sin^2(2\theta_{me})(\theta_m-\theta_{me})^2/\left[8K+\pi AR\sin^2(2\theta_{me})\right]. \qquad [2]$$

We were able to vary θ_{me} between 10–65° by adjusting details of the silica coating and polyethylene glycol (PEG) functionalization that alter the density of the polymer brushes grafted on the FNP surfaces (19, 20). This control of θ_{me} is consistent with the fact that direct surface functionalization of FNPs without silica coating yields perpendicular boundary conditions (10, 12) whereas a dense PEG functionalization of silica plates yields nearly tangential anchoring (Fig. S3). In the presence of **B**, the response of individual nanoplates is described by the corresponding energy $F_H = -\mathbf{m}\cdot\mathbf{B}$. In dilute FNP dispersions, the distribution of **m** and nanoplate orientations due to the total potential energy is then $f(\theta_m) = C\exp[-(F_{se}+F_H)/k_BT]$, where k_B is the Boltzmann constant, T is absolute temperature, and the coefficient C is found from ensuring $\int_0^\pi C\exp[-(F_{se}+F_H)/k_BT]\sin\theta_m d\theta_m = 1$. This field-dependent angular distribution, along with measured material parameters (*Supporting Information* and Fig. S4), allows us to model experimental absorbance spectra (Fig. 1 *E* and *F*). At fields ~1 mT perpendicular to $\mathbf{n}_0$, the individual FNPs first rotate on the cone of easy orientations to lower F_H while keeping θ_m close to θ_{me} and F_{se} near its minimum (Fig. 3 *B* and *C*), with the departure $\theta_m - \theta_{me} \approx 4°$ determined by a balance of elastic, surface anchoring, and magnetic torques originating from the angular dependencies of F_{se} and F_H. These tilted orientations of individual FNPs are consistent with self-diffusion of nanoplates probed by dark-field video microscopy (Fig. S2 and Movie S1).

Applied fields alter the distribution of FNP orientations (Fig. 1 *E* and *F* and Fig. S4) in a dilute dispersion, prompting additional distortions of the director around individual FNPs. The response of the composite to **B** both along and perpendicular $\mathbf{n}_0$ is paramagnetic-like and thresholdless (Fig. S5). For example, the field-induced birefringence and phase retardation ~π in homeotropic cells with $\mathbf{n}_0$ orthogonal to substrates (Fig. S5) is a result of the superposition of weak director distortions prompted by small rotations of individual FNPs in the dilute dispersion. Even the Earth's magnetic field of ~0.05 mT can rotate such nanoplates in LC to $\theta_m - \theta_{me} \approx 0.3°$. At strong fields ~20 mT, however, the individual FNPs rotate to large angles, so that their moments **m** approach the orientation of **B** and rotation-induced **n**(**r**) distortions slowly decay with distance away from them (Fig. 3*D*). The distorted **n**(**r**) can have two mutually opposite local tilts induced by rotations of nanoplates dependent on the initial alignments of **m** on the up- or down-cones (Fig. 3 *C*–*H*). These distortions prompt elastic interactions between the nanoplates, attractive for the same tilts and repulsive for the opposite ones (Fig. 3 *E*–*H*). Elastic interactions thus separate the nanoplates into domains with magnetic moments **m** that have the same up- or down-cone orientations (Fig. 4). For example, strong fields $\mathbf{B}\perp\mathbf{n}_0$ (~20 mT) rotate nanoplates and local **n**(**r**) in a cell with initial $\mathbf{n}_0$ perpendicular to substrates, causing elastic interactions and formation of ferromagnetic "drops" (localized regions with an increased density of FNPs with the same up-cone or down-cone orientations) when starting from low initial concentrations of nanoplates <0.5 wt % (Fig. 4 *A*–*C*). Spatially continuous ferromagnetic domains with **M** on up- or down-cones emerge in response to the same fields when starting from initial concentrations >0.5 wt % (Fig. 4 *D*–*F*). High-resolution dark-field video microscopy monitors kinetics of changes of the local number density of nanoplates in response to **B** (Fig. 4 *G*–*I*), until the interparticle separation becomes smaller than the optical resolution (Fig. 4*G*). FNP dispersions remain stable after prolonged application of strong fields.

Electrostatic charging of nanoplates in the LC with large Debye screening length λ_D = 0.3–0.5 µm (21) leads to long-range screened electrostatic repulsions. This agrees with video microscopy

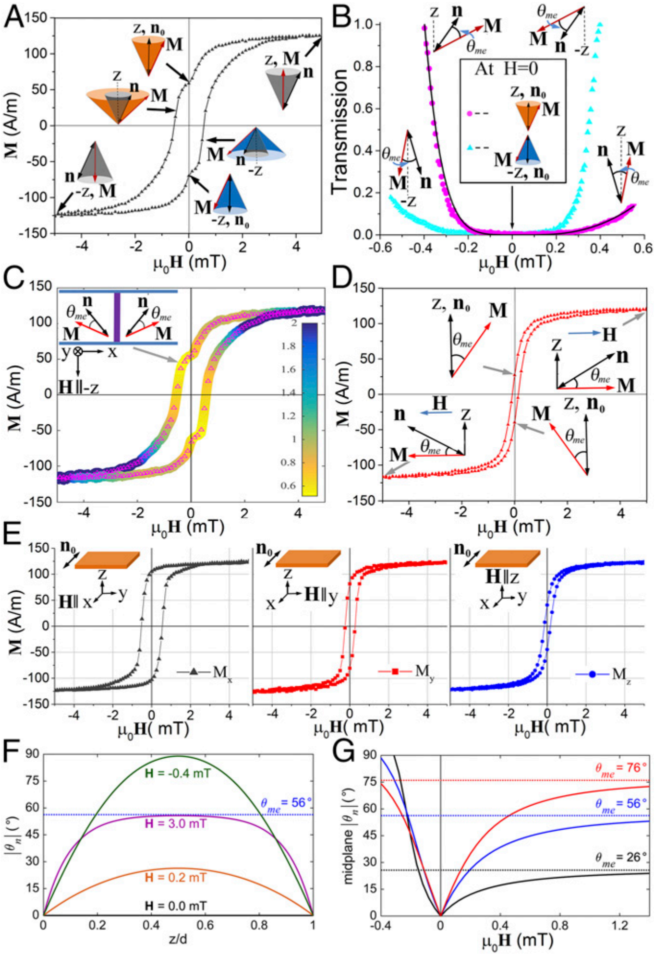

Fig. 2. Magnetic hysteresis and switching of BFLCCs. (*A*) Experimental hysteresis loop measured along $\mathbf{n_0}$ in a homeotropic cell. Schematics show orientations of **M** and **n**. (*B*) Experimental (symbols) and computer-simulated (black solid curve) light transmission of an aligned single-domain BFLCC between crossed polarizers in a cell with $\mathbf{n_0}$ and **H** normal to substrates. (*C*) Computer-simulated hysteresis loop for a BFLCC with domains (top left inset) fitted to experimental data (triangles) by varying the color-coded (right-side inset) lateral size to cell thickness ratio from 0.5 to 2. (*D*) Hysteresis loop probed for the same cell as in *A* but for $\mathbf{H}\perp\mathbf{n_0}$. (*E*) Hysteresis in a planar BFLCC cell for **M** along *x*, *y*, and *z* axes (*Insets*). (*F* and *G*) Computer-simulated (*F*) depth profiles of $|\theta_n|$ in a homeotropic cell of thickness $d = 60$ μm at different fields (note that, due to strong boundary conditions for **n** at the confining substrates, BFLCC cells with smaller *d* require stronger fields for switching) and (*G*) field dependencies of the maximum-tilt $|\theta_n|$ in the cell midplane for different θ_{me}. Computer simulations are described in *Supporting Information*.

observations that individual nanoplates rarely approach each other to distances smaller than 0.5–1 μm, even in fields ~5 mT applied in different directions (Fig. S6). The pair potential U_{elect} due to the screened Coulomb electrostatic repulsion between FNPs modeled as spheres of equivalent radius *R* is

$$U_{elect}(r_{cc}) = (A_1/r_{cc})\exp(-r_{cc}/\lambda_D), \qquad [3]$$

where r_{cc} is the center-to-center pair-separation distance, $\lambda_D = (\varepsilon\varepsilon_0 k_B T/2N_A e^2 I)^{-1/2}$, ε is an average dielectric constant of the LC, ε_0 is vacuum permittivity, N_A is the Avogadro's number, *I* is the ionic strength, $A_1 = (Z^*e)^2\exp(2R/\lambda_D)/[\varepsilon_0\varepsilon(1+R/\lambda_D)^2]$, and Z^* is the number of elementary charges on a single FNP. For $2R \approx 140$ nm, $Z^* \approx 500$, $\varepsilon \approx 11.1$, and $\lambda_D \approx 378$ nm (21), one finds $A_1 \approx 6.8 \times 10^{-23}$ J/m. Minimization of free energy of the elastic distortions induced by FNPs leads to an elastic pair-interaction potential that contains monopole and highly anisotropic dipolar and quadrupolar terms dependent on magnetic field intensity **H**:

$$U_{elast}(r_{cc}) = A_2/r_{cc} + A_3(\phi)/r_{cc}^{\,3} + A_4(\phi)/r_{cc}^{\,5}, \qquad [4]$$

where A_2, A_3, and A_4 are coefficients describing the elastic monopole, dipole, and quadrupole and ϕ is an angle between the center-to-center pair-separation vector $\mathbf{r_{cc}}$ and $\mathbf{n}_0$ (22). The magnetic pair potential due to moments $\mathbf{m}_1$ and $\mathbf{m}_2$ of FNPs is

$$U_m(r_{cc}) = \frac{\mu_0}{4\pi}\frac{1}{r_{cc}^{\,3}}\left[\mathbf{m}_1\cdot\mathbf{m}_2 - \frac{3(\mathbf{m}_1\cdot\mathbf{r}_{cc})(\mathbf{m}_2\cdot\mathbf{r}_{cc})}{r_{cc}^{\,2}}\right], \qquad [5]$$

where μ_0 is vacuum permeability. Superposition of Eqs. **3**–**5** gives the total interaction potential:

$$U(r_{cc}) = U_{elect}(r_{cc}) + U_m(r_{cc}) + U_{elast}(r_{cc}). \qquad [6]$$

At $r_{cc} \geq 400$ nm, corresponding to FNP dispersions up to 0.8 wt % (close to the initial concentration yielding continuous magnetic domains), magnetic pair interactions between the 140- × 7-nm nanoplates with dipoles $\sim 4 \times 10^{-17}$ Am^2 are weak, with $U_m \leq 1\, k_B T$. For larger FNPs (*Supporting Information* and Fig. S1) with magnetic moments up to $\sim 17 \times 10^{-17}$ Am^2 and at higher concentrations of FNPs, U_m including many-body effects overcomes the strength of thermal fluctuations, producing spatial patterns of domains. In Eq. **4**, the first monopole term is nonzero only at **B** pointing away from orientations of **m** that minimize F_{se}. The dipolar and quadrupolar

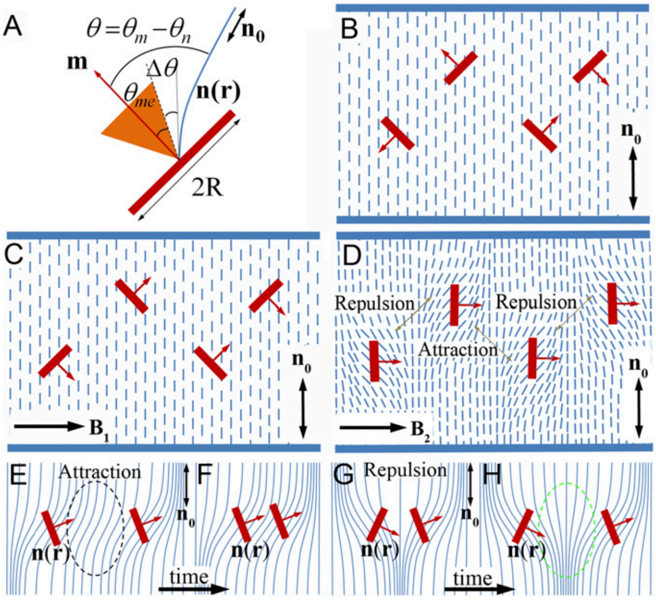

Fig. 3. Alignment, rotation, and elastic interactions between magnetically torqued FNPs in LCs. (*A*) Free-energy minimization for an FNP with finite conically degenerate boundary conditions, with **n(r)** distorted around the nanoplate and deviating by an angle $\Delta\theta$ from the easy axis orientation at its surface. (*B*) Equilibrium alignment of representative FNPs at B = 0 in a homeotropic cell. (*C*) Response of the original four FNPs to a very weak field B_1 ~0.1 mT, at which the nanoplates rotate mostly on the cone of low-energy orientations. (*D*) Rotation of FNPs in field B_2 ~10 mT that induces monopole-type elastic distortions with the **n(r)** tilt determined by the initial orientation of **m** on the up- or down-cone. (*E*–*H*) Minimization of elastic energy due to FNP-induced distortions prompts long-range interactions (*E* and *F*) attractive for nanoplates with like-tilted **n(r)** and (*G* and *H*) repulsive for FNPs with oppositely tilted **n(r)**. Elastic energy of director distortions (dashed ellipsoid in *E*) lowers with decreasing distance between like-tilted nanoplates (*F*) and is relieved (*G* and *H*) with increasing distance between oppositely tilted FNPs due to incompatible distortions they induce (dashed ellipsoid in *H*).

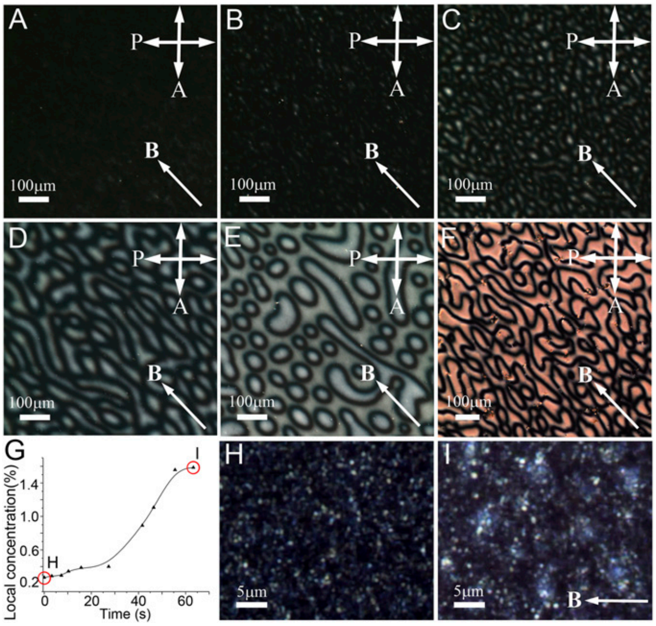

Fig. 4. Concentration-dependent behavior of FNP-LC dispersions. (*A*–*F*) POM micrographs showing a cell with initial homeotropic $\mathbf{n}_0$ for the following FNP concentrations and applied fields: (*A*) 0.07 wt %, B = 20 mT, (*B*) 0.13 wt %, B = 20 mT, (*C*) 0.27 wt %, B = 2 mT, (*D*) 0.53 wt %, B = 2 mT, (*E*) 1.07 wt %, B = 2 mT, and (*F*) 1.54 wt %, B = 2 mT. (*G*) Changes of local concentration with time in a field of 20 mT applied orthogonally to $\mathbf{n}_0$ of a homeotropic cell. (*H* and *I*) Dark-field micrographs corresponding to 0-s and 63.3-s data points marked by red circles in *G*. The concentration keeps changing at higher fields and longer elapsed times but tracking FNPs at internanoplate distances <400 nm is limited by optical resolution. Orientations of **B**, polarizer (P), and analyzer (A) are marked on images.

terms are always present due to symmetry of elastic distortions induced by the geometrically complex FNPs (Fig. 1*B* and Fig. S1) tilted with respect to $\mathbf{n}_0$. The elastic dipole and quadrupole terms help maintain correlated orientations of FNPs and their magnetic moments upon formation of BFLCCs in concentrated dispersions. When **B** rotates the nanoplates, the dominant elastic interactions are of the monopole type, mediating the formation of ferromagnetic "drops" as the local density of nanoplates is increased starting from low initial volume fractions (Fig. 4 *A*–*C*) and of continuous domains when starting from higher initial concentrations >0.5 wt % (Fig. 4 *D*–*I*). Aggregation of nanoplates is prevented by weakly screened repulsive U_{elect}. Short-term 5- to 50-s application of a field ~20 mT or, alternatively, prolonged application of weak fields <1 mT separates the FNPs in concentrated dispersions into domains that exhibit polar switching.

As in uniaxial ferromagnetic LC dispersions (7, 8, 9–12), preparation of BFLCCs can involve quenching of the LC host from the isotropic phase in an external **B**, which can produce up-cone or down-cone orientation of **M** within the entire sample. Alternatively, polydomain BFLCCs are obtained from a paramagnetic colloidal dispersion with initially random up- and down-cone orientations of **m** of FNPs by applying **B** to separate them into a sample of multidomains of opposite cone orientation (Fig. 5 and Movie S2), as shown using a sequence of micrographs in Fig. S7. The paramagnetic dispersion with random up- and down-cone orientations of FNPs is long-term unstable with respect to formation of ferromagnetic domains due to Earth's and ambient magnetic fields. By applying B~20 mT, a polydomain sample with up- and down-cone domains can be transformed to a monodomain BFLCC with the **M**-cone orientation matching the direction of applied field $\mathbf{B}\|\mathbf{n}_0$, as well as reversed by then reversing **B** to the opposite (Fig. S8). Switching **M** between up- and down-cones involves singular defects in $\mathbf{n}(\mathbf{r})$ visible in polarized optical microscopy (POM) (Fig. S8). Interestingly, even for **M** oriented on the same up- or down-cone within the entire sample, one observes spontaneous spatial variations of $\mathbf{M}(\mathbf{r})$, leading to a structure (Fig. 6) dubbed "left-right domains" with different tilts of **M** selected from the degeneracy of states of the same up- or down-cone.

BFLCCs are modeled using a continuum description invoking minimization of the total free energy composed of elastic, magnetic, and coupling terms [assuming that the boundary conditions for $\mathbf{n}(\mathbf{r})$ on confining cell substrates are infinitely strong and neglecting spatial gradients of the FNPs density]:

$$F = F_{elast} + F_{mag} + F_{coupl}. \qquad [7]$$

The elastic energy due to the spatial gradients of $\mathbf{n}(\mathbf{r})$ is

$$F_{elast} = \frac{1}{2}\int \left\{K_{11}(\nabla\cdot\mathbf{n})^2 + K_{22}(\mathbf{n}\cdot\nabla\times\mathbf{n})^2 + K_{33}[\mathbf{n}\times(\nabla\times\mathbf{n})]^2\right\}dV, \qquad [8]$$

where K_{11}, K_{22}, and K_{33} are the Frank elastic constants (Table S1) corresponding to splay, twist, and bend deformations, respectively. The magnetic term $F_{mag} = -\int \mu_0 \mathbf{M}\cdot\mathbf{H}_{total}dV$ describes the response of the BFLCC to external field **H** altered by the demagnetizing field, $\mathbf{H}_{total} = \mathbf{H} - D\mathbf{M}$, where we neglect the diamagnetic term and the direct interaction of $\mathbf{n}(\mathbf{r})$ and **H**, and D is the demagnetization factor dependent on the sample

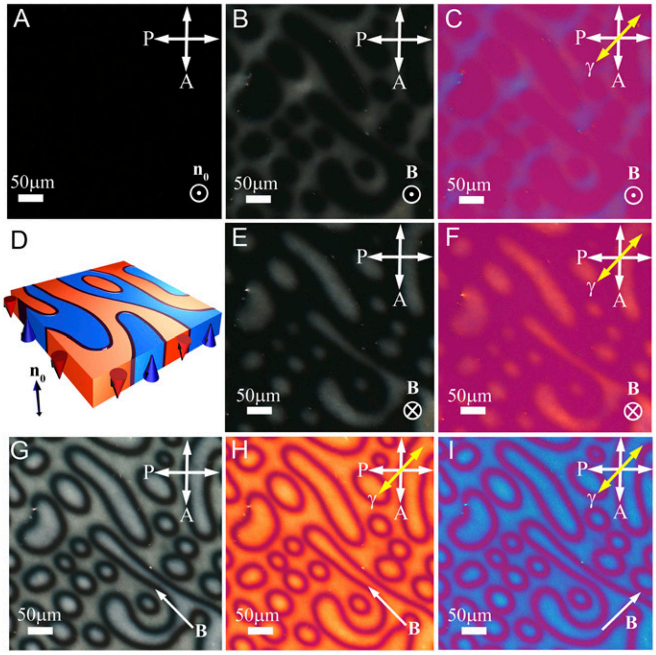

Fig. 5. Up-down domains in a homeotropic cell. (*A*–*C*) POM micrographs obtained (*A*) without **B** and (*B* and *C*) for $\mathbf{B}\|\mathbf{n}_0$ (B = 2 mT) (*B*) without and (*C*) with a 530-nm phase retardation plate inserted between crossed P and A, with its slow axis γ shown using a yellow double arrow. The POM micrograph in *A* appears dark because of the light propagation along $\mathbf{n}_0$ and weak optical biaxiality of BFLCCs. (*D*) Schematic of up-down domains and walls. (*E* and *F*) POM images of domains at **B** in the opposite direction (B = −2 mT) (*E*) without and (*F*) with the retardation plate. Complementary POM micrographs *B* and *C* and *E* and *F* originate from highly asymmetric response of the up- and down-cone domains to opposite vertical fields. (*G*–*I*) POM micrographs of domains at $\mathbf{B}\perp\mathbf{n}_0$ (B = 2 mT) (*G*) without and (*H* and *I*) with the retardation plate.

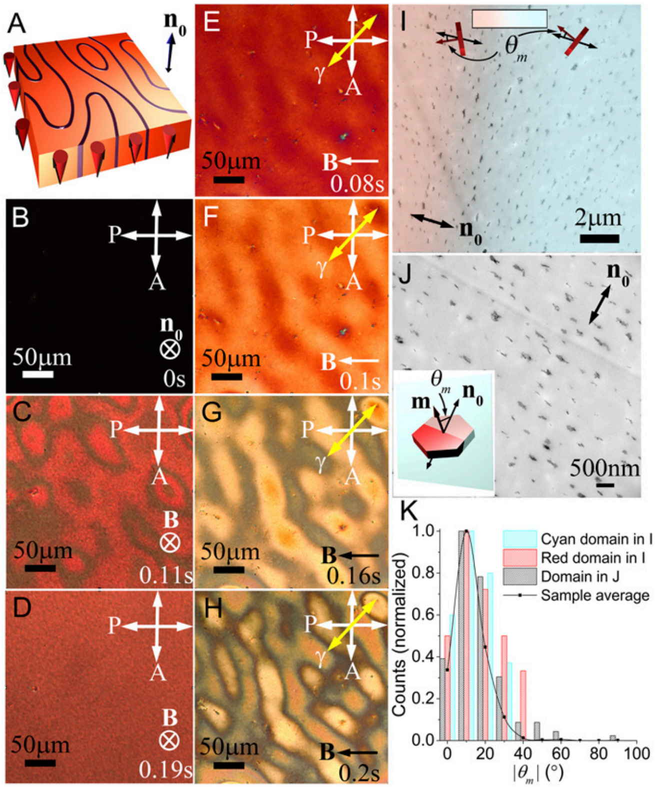

Fig. 6. Left-right domains in a homeotropic cell. (*A*) Schematic of the domains and walls. (*B*–*D*) POM images at (*B*) B = 0 and (*C* and *D*) at $\mathbf{B}\|\mathbf{n_0}$ (B = 2 mT). (*E*–*H*) POM images of domains at $\mathbf{B}\perp\mathbf{n_0}$ (B = 2 mT) with a 530-nm retardation plate with a slow axis γ (yellow double arrow) inserted between the crossed P and A. The elapsed time is marked on images. (*I* and *J*) TEM images of FNPs in a polymerized BFLCC for two microtome cutting planes parallel to $\mathbf{n_0}$, with the image in *I* containing **M** and that in *J* orthogonal to *I*. The inset in *I* shows coloring of the domains with differently tilted **m** (brown arrows) with respect to $\mathbf{n_0}$ (black double arrows). The cross-sections of obliquely sliced FNPs in *J* reveal their tilt with respect to the image plane and $\mathbf{n_0}$ (*Inset*). (*K*) Distribution of orientations of **m** measured using TEM images.

and field geometry as well as on the domains. The free energy term describing the coupling between $\mathbf{n}(\mathbf{r})$ and $\mathbf{M}(\mathbf{r})$ reads

$$F_{coupl} = \xi\int\left(\cos^2\theta_m - \cos^2\theta_{me}\right)^2 dV \approx \xi\sin^2(2\theta_{me})\int(\theta_m - \theta_{me})^2 dV, \qquad \textbf{[9]}$$

where the coupling coefficient ξ originates from the mechanical coupling of individual FNP orientations to **n**, enhanced by their collective response in concentrated dispersions.

Different free energy terms often compete, with the elastic term tending to minimize $\mathbf{n}(\mathbf{r})$ distortions, the magnetic term rotating **M** toward **B** while also prompting formation of domains due to the demagnetizing factor, and the coupling term tending to keep relative orientations of $\mathbf{n}(\mathbf{r})$ and $\mathbf{M}(\mathbf{r})$ at $\theta_m = \theta_{me}$. Numerical minimization of the free energy given by Eq. **7** yields equilibrium $\mathbf{n}(\mathbf{r})$ and $\mathbf{M}(\mathbf{r})$ at different fields consistent with the experimental hysteresis and switching data (Fig. 2 *A*–*C*). Allowing the magnetic domain size to be a fitting parameter, we model fine details of experimental hysteresis loops, such as the shoulder-like features in the vicinity of $\mathbf{B} = 0$ (Fig. 2*C*) and domain size behavior (Figs. 5 and 6). This modeling shows that BFLCC domains are governed by the competition between the demagnetizing and elastic free energy terms that exhibit rich behavior when the direction and strength of **B** are varied. The facile threshold-free polar switching of light transmission through a single-domain BFLCC between crossed polarizers (Fig. 2*B*) is consistent with the highly asymmetric tilting of **n** at different θ_{me} (Fig. 2 *F* and *G*).

To understand the richness of BFLCC domain structures, we carried out optical studies (Figs. 4–8 and Figs. S7–S9) and direct imaging of FNP orientations within domains with transmission electron microscopy (TEM) of polymerized and microtome-sliced BFLCCs (Fig. 6 *I* and *J*). The up-down domains, in which **M** lives on two opposite cones $\theta_m = \theta_{me}$, can be observed in homeotropic cells with $\mathbf{n}_0$ orthogonal to substrates (Fig. 5) and also in planar cells with in-plane $\mathbf{n}_0$ (Fig. 7). A magnetic holonomic control system (Fig. S2*A*), integrated with an optical microscope, allows us to apply **B** in arbitrary directions, at different tilts with respect to confining plates and different azimuthal orientations, and thus to probe the nature of BFLCC domains (Figs. 5–7). The response of coexisting domains is always present, except when $\mathbf{B}\|\mathbf{M}$ on the $\theta_m = \theta_{me}$ cones, consistent with the C_s symmetry of BFLCCs. The switching of up- and down-cone domains by $\mathbf{B}\|\mathbf{n}_0$ is thresholdless (similar to that shown in Fig. 2*B*), highly asymmetric (polar), and complementary for the two antiparallel directions of **B**, so that the different domains can be distinguished (Figs. 5 *A*–*F* and 7). Up- and down-cone domains in homeotropic cells respond equally strongly to in-plane **B** (Fig. 5 *G*–*I*), although the director within neighboring domains tilts in opposite directions, with homeotropic $\mathbf{n}(\mathbf{r})$ in the walls in between. In planar cells, rotations of the in-plane **B** and the sample between crossed polarizers in POM reveal distorted $\mathbf{n}(\mathbf{r})$ and $\mathbf{M}(\mathbf{r})$ within the domains (Fig. 7).

BFLCCs prepared to have **M** on the up- or down-cone within the entire sample slowly develop the left-right domains with different azimuthal orientations of **M** on the same cones (Fig. 6), separated by analogs of Bloch walls (23) across which **M** continuously rotates. The presence of left-right domains becomes apparent with **B** applied at angles to $\mathbf{n}_0$ different from θ_{me}, including that normal to substrates of a homeotropic cell (Fig. 6 *B*–*D*), revealing domains due to their different tilting and then making the sample appear uniform again in **B** that aligns **M** roughly along the cell normal. Reversing or applying in-plane **B** makes this "left-right" domain structure visible again due to different rotations of **M** within the domains (Fig. 6 *E*–*H*). Ferromagnetic domains of both up-down and left-right types are also probed by polymerizing BFLCCs at B = 0 and then directly imaging

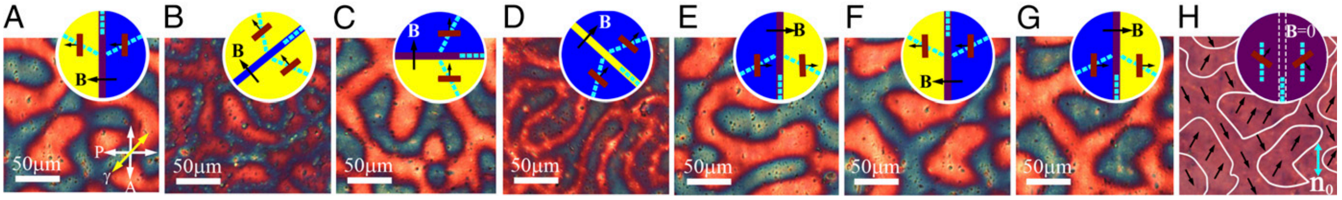

Fig. 7. Up-down domains in a planar cell. POM images obtained with the 530-nm plate (γ) inserted between crossed P and A for **B** (B = 2 mT) orthogonal to the rubbing direction $\mathbf{n_0}$ at (*A*) 0°, (*B*) 45°, (*C*) 90°, (*D*) 135°, and (*E*) 180° with respect to P, (*F* and *G*) before and after reversing **B** and (*H*) at B = 0. Dashed cyan lines in insets show $\mathbf{n}(\mathbf{r})$. White lines in *H* depict walls between domains with uniform $\mathbf{n_0}$ and different **M**-orientations marked by arrows.

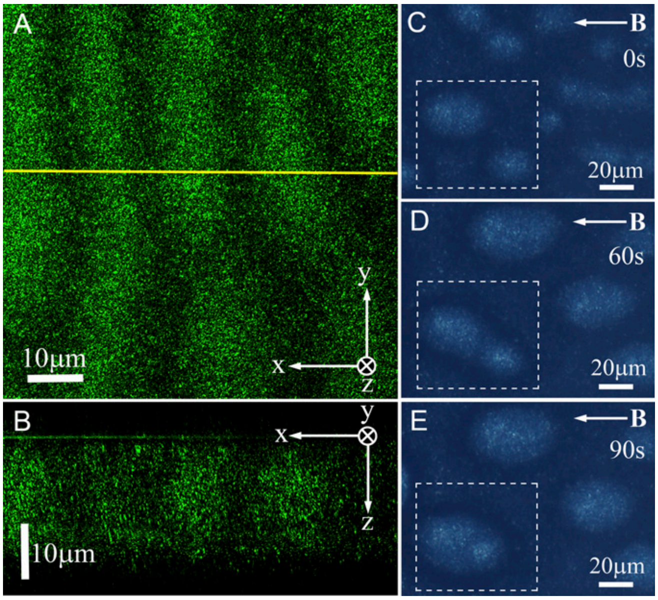

Fig. 8. Three-dimensional structure and dynamics of up-down domains. (*A* and *B*) Fluorescence confocal images of the BFLCC with FNPs labeled with dye at B = 0 obtained (*A*) for the cell midplane and (*B*) in a cross-section along the yellow line in *A*. (*C–E*) Domain interactions and merging (within dashed squares) in a homeotropic cell at $\mathbf{B}\perp\mathbf{n}_0$ (B = 30 mT) probed with dark-field microscopy and scattering from FNPs. Elapsed time is marked on images.

orientations of nanoplates with TEM (Fig. 6 *I–K*), revealing θ_{me} of individual FNPs and **M** tilted relative to $\mathbf{n}_0$.

Three-dimensional confocal fluorescence (Fig. 8 *A* and *B*) and dark-field microscopies (Fig. 8 *C–E*) and bright-field imaging in a transmission mode that derives contrast from spatially varying absorption of BFLCCs (Fig. S9) provide insights into the spatial changes of local number density of nanoplates. Upon formation of up-down domains, the concentration of nanoplates is depleted in the interdomain walls and increased within the domain regions (Fig. 8 and Fig. S9), becoming more homogeneous again when **B** is turned off. The ensuing walls (Figs. 5, 7, and 8) between the up-down domains with decreased magnitude of **M** and an abrupt change of its orientation differ from the common Bloch and Néel walls with a solitonic continuous change of **M**-orientation (23). The Bloch-like walls between the left-right domains with **M** on up- or down-cone with respect to $\mathbf{n}_0$ (Fig. 6) have uniform number density of FNPs and localized changes of **M**-orientation (23).

To conclude, we have introduced a soft-matter system of BFLCCs with the C_s symmetry that combines 3D fluidity and biaxial orientational ordering of constituent molecular and colloidal building blocks. We have identified diverse domain structures and unusual polar switching of BFLCCs. We envisage a rich variety of new fundamental behavior that remains to be probed, such as formation of different topological defects. We also foresee practical uses enabled by threshold-free response of BFLCCs to weak magnetic fields.

Materials and Methods

Barium hexaferrite $BaFe_{11.5}Cr_{0.5}O_{19}$ FNPs were synthesized by the hydrothermal method and then coated with SiO_2 (*Supporting Information*). These nanoplates were surface-functionalized by trimethoxysilane-PEG (JemKem Technology). Some FNPs were fluorescently labeled with fluorescein isothiocyanate (Sigma-Aldrich). To disperse FNPs in LCs, pentylcyanobiphenyl (5CB; Chengzhi Yonghua Display Materials Co. Ltd.) was mixed with 0.01–20 wt % FNPs in methanol, followed by solvent evaporation at 90 °C for 3 h. The sample was rapidly cooled to the nematic phase of 5CB while vigorously stirring it. The ensuing composite was centrifuged at 500 × *g* for 5 min to remove residual aggregates and leave only well-dispersed FNPs (10). For fluorescence confocal microscopy, FNPs labeled with the dye were mixed with unlabeled ones in a 1:50 ratio, so the individual labeled FNPs could be resolved. We used TEM CM100 (Philips) for nanoscale imaging. BFLCCs were controlled by a three-axis electromagnetic holonomic manipulation apparatus mounted on a microscope (Fig. S2*A*). POM of BFLCCs used microscopes BX-51 and IX-81 (Olympus) equipped with 10×, 20×, and 50× dry objectives with N.A.s of 0.3–0.9 and a CCD camera (Spot 14.2 Color Mosaic; Diagnostic Instruments, Inc.). Dark-field imaging additionally used an oil-immersion dark-field condenser (N.A. ≈1.4) and a 100× air objective (N.A. ≈0.6). Video microscopy used a Point Gray camera FMVU-13S2C-CS. Particle dynamics was analyzed by ImageJ software (NIH). Absorbance spectra were obtained using a spectrometer USB2000-FLG (Ocean Optics) integrated with a microscope. Fluorescence confocal imaging used the inverted IX-81 microscope, the Olympus FV300 laser-scanning unit, and a 488-nm excitation laser (Melles Griot). A 100× oil objective with N.A. of 1.42 was used for epidetection of the confocal fluorescence within a 515- to 535-nm spectral range by a photomultiplier tube. Magnetic hysteresis was characterized in 4- × 4- × 0.06-mm homeotropic and planar glass cells (Fig. 2) using an alternating gradient magnetometer (MicroMag 2900; Princeton Measurement Corp.) and a vibrating sample magnetometer (PPMS 6000; Quantum Design).

ACKNOWLEDGMENTS. We thank N. Clark, L. Jiang, H. Mundoor, and B. Senyuk for discussions and C. Ozzello, T. Giddings, M. Keller, A. Sanders, Q. Zhang, and Y. Zhang for assistance. This work was supported by US Department of Energy, Office of Basic Energy Sciences, Division of Materials Sciences and Engineering Award ER46921 (to Q.L., P.J.A., and I.I.S.), the US National Science Foundation Grant DMR-1120901 (to T.C.L.), and a Simons Fellows grant (to T.C.L.).

1. de Gennes PG, Prost J (1995) *The Physics of Liquid Crystals* (Clarendon, Oxford).
2. Luckhurst GR, Sluckin TJ, eds (2015) *Biaxial Nematic Liquid Crystals: Theory, Simulation and Experiment* (Wiley, Chichester, UK).
3. Born M (1916) Über anisotrope Flüssigkeiten. Versuch einer Theorie der flüssigen Kristalle und des elektrischen Kerr-Effekts in Flüssigkeiten. *Sitz Kön Preuss Akad Wiss* 30:614–650.
4. Ilg P, Odenbach S (2009) *Colloidal Magnetic Fluids: Basics, Development and Application of Ferrofluids*, ed Odenbach S (Springer, Berlin), pp 249–326.
5. Albrecht T, et al. (1997) First observation of ferromagnetism and ferromagnetic domains in a liquid metal. *Appl Phys A Mater Sci Process* 65(2):215–220.
6. Brochard F, de Gennes PG (1970) Theory of magnetic suspensions in liquid crystals. *J Phys* 31(7):691–708.
7. Rault J, Cladis PE, Burger JP (1970) Ferronematics. *Phys Lett A* 32(3):199–200.
8. Chen S-H, Amer NM (1983) Observation of macroscopic collective behavior and new texture in magnetically doped liquid crystals. *Phys Rev Lett* 51(25):2298–2301.
9. Mertelj A, Lisjak D, Drofenik M, Copič M (2013) Ferromagnetism in suspensions of magnetic platelets in liquid crystal. *Nature* 504(7479):237–241.
10. Zhang Q, Ackerman PJ, Liu Q, Smalyukh II (2015) Ferromagnetic switching of knotted vector fields in liquid crystal colloids. *Phys Rev Lett* 115(9):097802.
11. Mertelj A, Osterman N, Lisjak D, Copič M (2014) Magneto-optic and converse magnetoelectric effects in a ferromagnetic liquid crystal. *Soft Matter* 10(45):9065–9072.
12. Hess AJ, Liu Q, Smalyukh II (2015) Optical patterning of magnetic domains and defects in ferromagnetic liquid crystal colloids. *Appl Phys Lett* 107(7):071906.
13. Freiser MJ (1970) Ordered states of a nematic liquid. *Phys Rev Lett* 24(19):1041.
14. Miyajima D, et al. (2012) Ferroelectric columnar liquid crystal featuring confined polar groups within core-shell architecture. *Science* 336(6078):209–213.
15. Brand HR, Cladis PE, Pleiner H (2000) Polar biaxial liquid crystalline phases with fluidity in two and three spatial dimensions. *Int J Eng Sci* 38(9):1099–1112.
16. Lubensky TC, Radzihovsky L (2002) Theory of bent-core liquid-crystal phases and phase transitions. *Phys Rev E Stat Nonlin Soft Matter Phys* 66(3):031704.
17. Tschierske C, Photinos DJ (2010) Biaxial nematic phases. *J Mater Chem* 20(21):4263–4294.
18. Lagerwall JPF, Scalia G, eds (2016) *Liquid Crystals with Nano and Microparticles* (World Scientific, Singapore).
19. Love JC, Estroff LA, Kriebel JK, Nuzzo RG, Whitesides GM (2005) Self-assembled monolayers of thiolates on metals as a form of nanotechnology. *Chem Rev* 105(4):1103–1169.
20. Ramdane OO, et al. (2000) Memory-free conic anchoring of liquid crystals on a solid substrate. *Phys Rev Lett* 84(17):3871–3874.
21. Mundoor H, Senyuk B, Smalyukh II (2016) Triclinic nematic colloidal crystals from competing elastic and electrostatic interactions. *Science* 352(6281):69–73.
22. Stark H (2001) Physics of colloidal dispersions in nematic liquid crystals. *Phys Rep* 351(6):387–474.
23. Morrish AH (2001) *The Physical Principles of Magnetism* (IEEE, New York).
24. Graf C, Vossen DL, Imhof A, van Blaaderen A (2003) A general method to coat colloidal particles with silica. *Langmuir* 19(17):6693–6700.
25. Van Blaaderen A, Vrij A (1992) Synthesis and characterization of colloidal dispersions of fluorescent, monodisperse silica spheres. *Langmuir* 8(12):2921–2931.
26. Aharoni A (1998) Demagnetizing factors for rectangular ferromagnetic prisms. *J Appl Phys* 83(6):3432–3434.